ACS OMEGA

Open Access

http://pubs.acs.org/journal/acsodf

Article

Effect of Low-Temperature Plasma-Modified Carbon Fibers on Impact Load Damage of Low-Density Oil-Well Cement

Yong Ma, Jianhua Guo, Sen Liu, Yangsong Wang, Jingxuan Cai, and Xiaowei Cheng*

Cite This: *ACS Omega* 2024, 9, 7564−7574

Read Online

ACCESS | Metrics & More | Article Recommendations

ABSTRACT: After large-scale exploitation of conventional oil and gas resources, most remaining resources are in highly depleted zones, where the fracture pressure of the formations is greatly reduced. Low-density oil-well cement prevents wellbore and formation fractures by reducing annular liquid column pressure and is one of the most commonly used cements in the oil and gas industry. However, cement sheaths made of low-density oil-well cement can be easily damaged due to the impact load generated during the well completion process. Incorporating carbon fibers into the cement matrix can effectively enhance the performance of cement sheaths. To ensure that carbon fibers can be closely combined with the cement matrix, low-temperature plasma modification technology was used in this study to pretreat the fibers. The mechanical properties of low-density oil-well cement incorporated with unmodified or modified carbon fibers were studied in detail under an impact load. The results of X-ray photoelectron spectroscopy revealed that the content of hydrophilic groups on the surface increased from 18.3 to 60.3% after the plasma treatment. The impact test results showed that the peak strengths of the cements cured at 60 °C for 14 days with 0.3% unmodified and modified carbon fibers could reach 37.01 ± 1.7 and 62.27 ± 1.7 MPa, respectively, under the impact load, i.e., an increase of 68.25% after the carbon fibers were treated with low-temperature plasma. Similarly, the absorbed energy increased from 15.59 to 44.31 J, and the energy absorption rate increased from 25.98 to 73.85%. Low-temperature plasma modification provided hydrophilic functional groups on the surface, significantly improving the interfacial bonding between the carbon fibers and cement matrix. The strengthened interaction was beneficial to extending the bearing time under the impact load and demonstrated a positive influence on the mechanical properties related to the impact resistance.

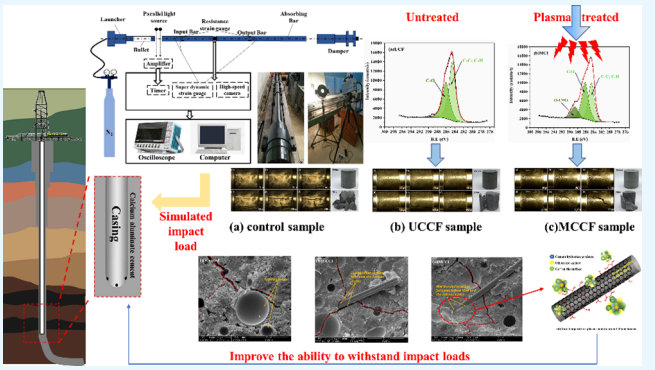

1. INTRODUCTION

Cementing is one of the most important steps in the exploitation of oil or gas.[1−3] The quality of cementing directly affects the oil and gas output as well as construction safety. Most existing conventional oil and gas resources are in highly depleted zones after large-scale exploitation,[4] where the fracture pressure of the strata is greatly reduced. The low-fracture-gradient and permeable strata in unconventional oil and gas resources[5,6] also increase the difficulty of cementing. Low-density oil-well cement[7,8] can complete the cementing operation by reducing the pressure of the annular liquid column. Thus, the ruptures caused by excessive cement slurry column pressure can be avoided in the weak formation area, reducing the drilling time and minimizing the potential pollution, reservoir damage, or severe incidents. It has been demonstrated that low-density oil-well cement systems have become some of the most commonly used cements in the oil and gas industry.

Under normal circumstances, the standard density of conventional Portland G-grade oil-well cement with a water-to-cement ratio of 0.44 is 1.89 g/cm^3. The density of a low-density oil-well cement system can be reduced to 0.7−1.80 g/cm^3.[9] Low-density cement systems can be divided into three categories:[10] water-expandable cement systems, foamed cement systems, and lightening-agent-containing cement systems. Water-expandable cement systems reduce the density of oil-well cement slurry by increasing the water−cement ratio and adding bentonite, fly ash, or sodium metasilicate as tackifiers to avoid excess free water.[11] Foamed cement systems[12] are obtained by uniformly filling ordinary cement slurry with nitrogen gas bubbles, and the stability of the cement slurry is highly dependent on the capacity and

Received: August 30, 2023
Revised: January 13, 2024
Accepted: January 29, 2024
Published: February 8, 2024

Table 1. Chemical and Mineral Compositions of Class G Oil-Well Cement (wt %)

	components												
	chemical composition									mineral composition			
	CaO	SiO_2	Fe_2O_3	Al_2O_3	SO_3	MgO	K_2O	Na_2O	loss	C_3S	C_2S	C_3A	C_4AF
content (%)	62.72	21.64	4.65	4.01	2.28	2.06	0.46	0.12	1.72	50.79	23.65	2.74	14.14

performance of the filling gas. However, it is challenging for these two cement systems to meet the service requirements of a high temperature and a high pressure in the well. Comparatively, a cement system with a lightening agent,[13] such as floating beads, has the advantage of a high bearing capacity and is also suitable for critical conditions.

A low-density cement containing floating beads generally has a low compressive strength. To improve its deformability and brittleness, cellulose fibers,[14,15] carbon fibers (CFs),[16] mineral fibers,[17] and synthetic high-molecular-weight polymers[18] have been successfully added to the cement matrix. By adding CFs,[19] lightweight cement can be obtained with a high strength, a high modulus, high-temperature resistance, corrosion resistance, and fatigue resistance. The static load compressive strength can also be improved. However, the interfacial bonding between CFs and the cement remains a challenge because of the low content of hydrophilic active groups on CFs.[20] To improve the bonding ability, surface treatment has been performed on CFs using acid and alkali solution immersion,[21] surface coating,[22] low-temperature plasma modification,[23,24] etc. These modification methods can etch the surface, provide a functional coating, or graft active groups onto the surface of CFs. With the change in surface roughness and physicochemical properties after modification, possible damage to the strength of CFs will also be induced.[25,26] Based on a comparison of a series of surface modification methods, low-temperature plasma treatment has the advantages of feasible functional group optimization, stable grafting properties, and less strength loss.

The low-density oil-well cement slurry is injected into the annulus between the formation and casing,[27] and the cement sheath stabilizes the well wall, protects the casing, and seals off the oil and gas water layers in the formation. However, the loss of integrity of the cement sheath will directly damage the sealing ability, and the water channeling between layers will seriously affect the life of oil and gas wells and cause economic loss. During the service period of the cement sheath, it not only bears the static pressure of the formation but also is subject to the impact load, for example, drilling tool vibration,[28] perforation impact during the well completion process,[29] and string vibration during oil production transportation.[30] An impact load with a short loading time and a fast energy release rate has a negative impact on the integrity of the cement sheath. However, most existing mechanical properties of cement are evaluated based on the static load, and only a few studies have been conducted under impact loads. The current work focuses on the mechanical properties of a floating bead oil-well cement system under an impact load.

In this study, CFs were pretreated using low-temperature plasma modification and incorporated into a low-density floating bead cement system. The properties of the surface groups on the CFs and the microscopic morphologies of the samples were studied. The relationship between the mechanical properties and energy evolution of cement stone was investigated through a split Hopkinson pressure bar impact test. Crack-derived pictures were obtained based on high-speed photography technology to examine the mechanical behavior of cement stone under an impact load. Finally, the mechanism was explored for the correlation between surface properties of CFs before and after low-temperature plasma modification and the resulting mechanical properties of the cement stones.

2. MATERIALS AND METHODS

2.1. Materials. The cement used in this research was grade G oil-well cement (Jiahua Special Cement Co., Ltd.). Its chemical composition and mineral composition are listed in Table 1. G33S (Weihui Chemical Co., Ltd.) was added as a fluid loss agent. The dispersants used in this study were USZ (Weihui Chemical Co., Ltd.), bleaching beads (Minnesota Mining and Machinery Manufacturing Company, United States), and microsilica (Chengdu Omike Petroleum Technology Co., Ltd.). The CFs were purchased from Beijing RongNair Engineering Materials, and their mechanical properties are listed in Table 2.

Table 2. Properties of CFs

ID	diameter (μm)	tensile strength (MPa)	elastic modulus (GPa)	elongation (%)	density (g/cm^3)
CFs	5−8	>3300	210−240	1.3−1.8	1.78

2.2. Experiment Preparation. The preparation of the cement pastes and curing of the specimens were performed according to the recommended methods in the API RP10B standard.[31] The experimental compositions of cement paste are listed in Table 3, and the water/cement ratio was maintained as 0.75. The cement slurry was placed in a metal mold with dimensions of φ50 mm × h50 mm. After the cement slurry solidified, the mold was removed to obtain a cylindrical stone sample. Three parallel samples were prepared for each formula. A total of 27 samples were cured in a water bath at 60 °C for 14 days. UCF and MCF represent CFs without and with low-temperature plasma treatment, respectively. The groups of cement samples with UCF and MCF were denoted as UCCF and MCCF, respectively.

2.3. Methods. *2.3.1. Low-Temperature Plasma Modification Treatment of CFs.* In this experiment, the CFs were modified by using a low-temperature plasma treatment apparatus (model DT-03, Suzhou Opus Plasma Co., Ltd.) operating at 80 W. The initial vacuum was set at 16 Pa. Oxygen was introduced as the plasma gas with a flow rate of 40 cm^3/min, and the treatment time was 60 s.

2.3.2. Split Hopkinson Pressure Bar Test. The dynamic load impact tests were performed using an AFT-0957 split Hopkinson rod with a rod diameter of 50 mm provided by the Central South University.[32−34] A schematic of the experimental setup is shown in Figure 1. The main components of the instrument are the incident rod, transmission rod, absorption rod, conical bullet, and acquisition system. All of the rods and bullets were composed of 40 Gr

https://doi.org/10.1021/acsomega.3c06486
ACS Omega 2024, 9, 7564−7574

Table 3. CF Low-Density Cement Formula (wt %)

ID	G-class oil-well cement (%)	floating beads (%)	microsilicon (%)	G33S (%)	USZ (%)	UCF (%)	MCF (%)	density (g/cm^3)
control	100	25	15	2	0.5			1.50
UCCF-0.2%	100	25	15	2	0.5	0.2		1.50
UCCF-0.3%	100	25	15	2	0.5	0.3		1.50
UCCF-0.4%	100	25	15	2	0.5	0.4		1.50
UCCF-0.5%	100	25	15	2	0.5	0.5		1.50
MCCF-0.2%	100	25	15	2	0.5		0.2	1.50
MCCF-0.3%	100	25	15	2	0.5		0.3	1.50
MCCF-0.4%	100	25	15	2	0.5		0.4	1.50
MCCF-0.5%	100	25	15	2	0.5		0.5	1.50

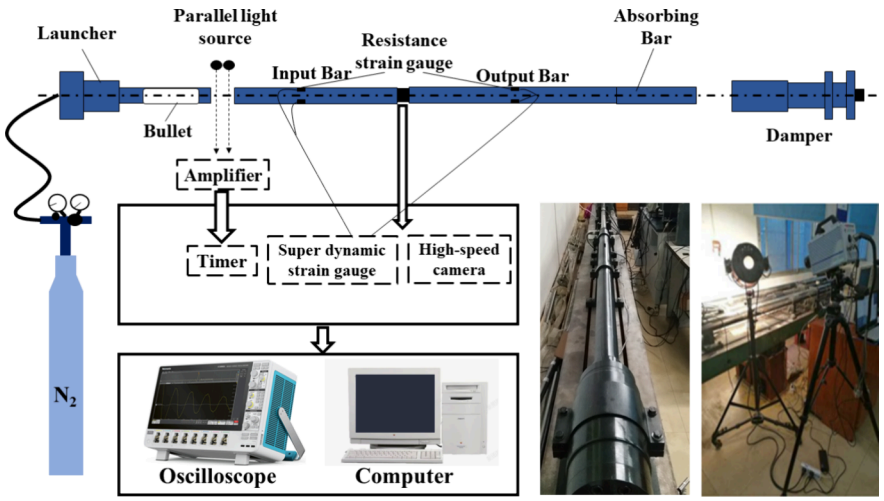

Figure 1. Split Hopkinson pressure bar test (SHPB) device diagram.

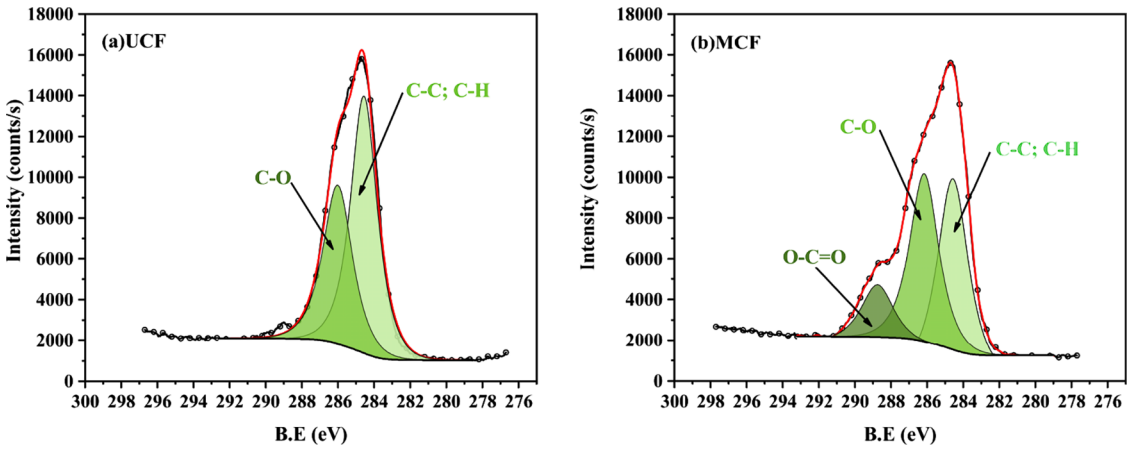

Figure 2. C 1s XPS spectra of (a) UCF and (b) MCF.

alloy steel. The rod density, longitudinal wave velocity, and elastic modulus were 7817 kg/m^3, 5458 m/s, and 233 GPa, respectively. The fixed impact pressure is 0.5 MPa, and the ejection velocity of the impactor is approximately 10 m/s. Experimental data were collected using a CS1D ultradynamic strain gauge, a DL750 endoscopic recorder, and a high-speed camera. A thin layer of Vaseline A was used to coat the cylindrical sample (diameter of 50 mm and height of 50 mm) to ensure that both ends were flat. Then, the sample was sandwiched between the incident and the transmission rods.

2.3.3. X-ray Photoelectron Spectroscopy. The surfaces of CFs before and after low-temperature plasma modification were measured with a PHI Quantum 2000 X-ray photoelectron spectroscopy (XPS) system equipped with a monochromatic Al (Kα) X-ray source. The working power was 25 W, the starting angle was 45° relative to the sample surface, and the analysis area was 500 μm × 400 μm. In the test, a combination of an electron gun and ion bombardment was used for charge compensation.

2.3.4. Scanning Electron Microscopy. After the dynamic load impact test, a fresh piece of the fractured cement sample was coated with a gold layer using an LDM150D vacuum ion sputtering instrument and was observed by environmental scanning electron microscopy (SEM) (Quanta 450, FEI Company).

https://doi.org/10.1021/acsomega.3c06486
ACS Omega 2024, 9, 7564−7574

3. RESULTS AND DISCUSSION

3.1. XPS Analysis of UCF/MCF. Figure 2a,b shows the C 1s XPS spectra of the CFs before and after modification, respectively. Table 4 summarizes the peak position and quantitative composition of each C group in UCF and MCF. Before the low-temperature plasma modification, two binding energy peaks at 284.62 and 286.00 eV were observed, corresponding to C−H/C−C and C−O, respectively. After the treatment, a new peak associated with O−C═O emerged at 288.75 eV. Comparing the compositions shown in Table 4, the plasma modification increased the carbonyl (−O−C═O−) or carboxyl (−COOH) groups on the surface, and the C−H/C−C binding mode reduced from 81.7 to 39.7%. The combination of C−O increased from 18.3 to 44.1%, and the ratio of O−C═O increased from 0 to 16.2%. The content of hydrophilic groups (C−O and O−C═O) on the surface of CFs[35,36] increased from 18.3 to 60.3%, and the hydrophilicity of the modified CFs was greatly improved.

Table 4. Peak Position and Quantitative Compositions of C-Containing Groups in UCF and MCF

	peak position (eV)			relative amount (%)		
fiber types	C−C, C−H	C−O	O−C═O	C−C, C−H	C−O	O−C═O
UCF	284.62	286.00		81.7	18.3	
MCF	284.60	286.15	288.75	39.7	44.1	16.2

When the high energy of the oxygen plasma bombarded the CFs surface, the ether bonds (−C−O−C−) were broken to form new alkyl groups ($-CH_n$) and hydroxyl groups (−OH). As the surface energy of the etched CFs increased, more free radicals were generated, leading to the formation of multiple hydroxyl (−OH) functional groups, which then were converted to more stable carbonyl (−O−C═O−) or carboxyl (−COOH) groups. These oxygen-containing groups had excellent hydrophilicity and could strengthen the interface between the CFs and cement matrix.

3.2. Mechanical Performance of UCCF/MCCF. Figure 3 shows the peak stress diagrams of UCCF and MCCF samples with different CF loadings. The peak stress under a dynamic load was analogous to the compressive strength under a static load.[37,38] Compared with the blank control, both UCCF and MCCF show an enhanced peak intensity. With the increase in the content of UCF and MCF in the cement paste, the peak strengths of UCCF and MCCF both increased first and decreased under the impact load. The peak strength of the blank control under the impact load was 12.16 ± 1.3 MPa. In comparison, the peak strength of UCCF-0.3% and MCCF-0.3% could reach 37.01 ± 1.7 and 62.27 ± 1.7 MPa, respectively, under the same impact load.

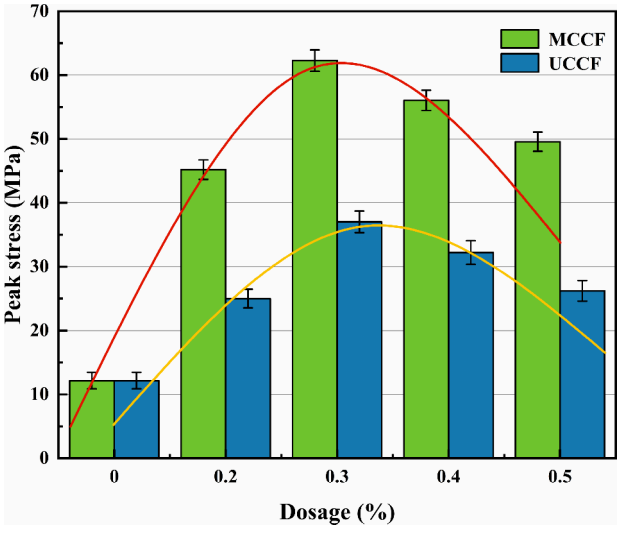

Figure 3. Peak stress diagram of cement specimens under impact loading.

Figure 4 shows the stress−strain curves of UCCF and MCCF samples with different CF loadings under impact loads. The peak stress and strain of the blank control without any CFs were relatively small, which agreed with the low-strength mechanical characteristics of the conventional floating bead low-density cement stone sample. The slope of the linearly rising section of the stress−strain curve was the stiffness characterizing the ability of the material to resist elastic deformation.[39] In Figure 4a, the stiffness and strength increased significantly when 0.2 or 0.3% UCF was incorporated into the cement matrix due to UCF's superior mechanical properties and large aspect ratio, suggesting that UCF acted as a skeleton in the cement base under an impact load. A high peak strength is related to a high overall stiffness under an impact load. However, when the UCF content increased to 0.5%, the strength and stiffness decreased significantly. This showed that excessive CFs led to a decrease in the mechanical properties.[40] In Figure 4b, the area enclosed by a stress−strain curve is the toughness characterizing the ability of the material to resist external loads.[41] The larger the enclosed area, the stronger is the ability to resist impact load damage.[42] After the UCF was modified by low-temperature plasma, more surface hydrophilic groups improved the bonding ability with the cement matrix. Therefore, the stiffness, strength, and toughness of the samples in the MCCF group were significantly increased. When the addition of MCF increased to 0.5%, although the overall stiffness was the largest, the toughness exhibited a significant decreasing trend. This showed that the loading of MCF was too large, which reduced the homogeneity in the cement matrix.[43] This, in turn, limited the ability to resist external impact, resulting in deterioration of mechanical properties under an impact load.

In summary, both UCF and MCF were external admixtures added to low-density floating bead cement with a low strength. The peak strength under an impact load was significantly improved. At the same time, low-temperature plasma modification increased the content of hydrophilic groups on the surface of CFs, which enhanced the bonding ability with the cement matrix, thereby increasing the overall peak strength of the material. However, when the amounts of UCF and MCF were too large, the mechanical properties of the samples decreased. The results showed that the optimal amount of UCF and MCF in the low-density floating bead cement system was 0.3%.

3.3. Dynamic Energy Evolution and Crack Derivation. *3.3.1. Dynamic Energy Evolution.* When an AFT-0957 split Hopkinson rod with a diameter of 50 mm impacted the sample at a speed of 10 m/s, the energy pulse required was only $2L_s/C_e$ back and forth because of the relatively small thickness of the sample, where C_e is the wave velocity of the Hopkinson pressure bar and L_s is the sample height of a cylindrical cement stone test specimen. After the energy pulse was reflected and

https://doi.org/10.1021/acsomega.3c06486
ACS Omega 2024, 9, 7564−7574

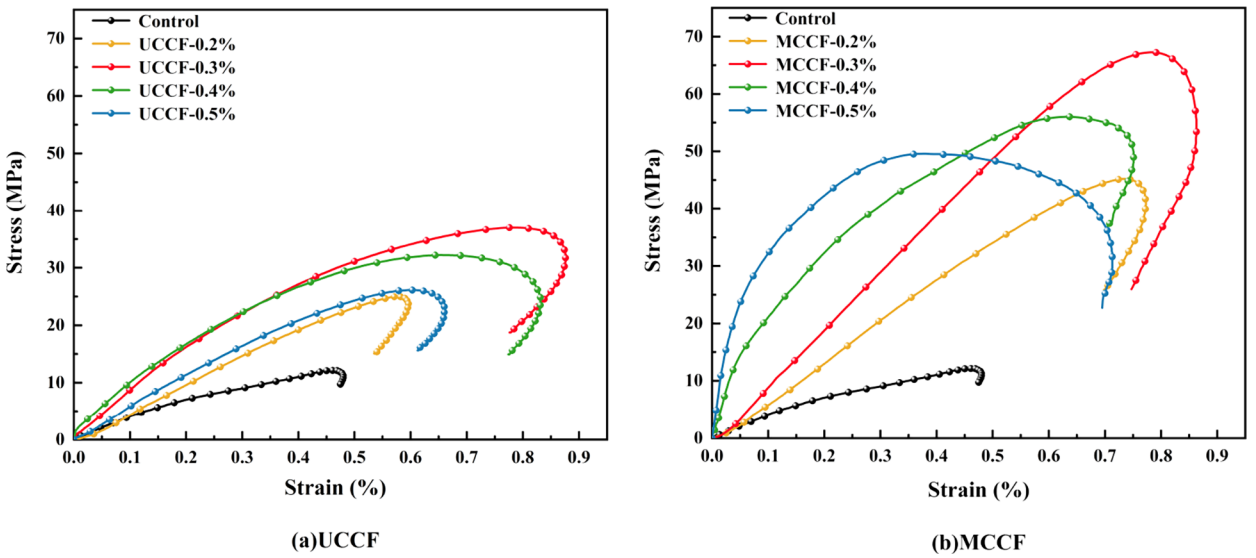

Figure 4. Stress−strain curves of (a) UCCF and (b) MCCF under impact loading.

transmitted multiple times, the stress and strain on both ends of the sample were basically the same. The transient waveform recorded the incident wave stress $\sigma_I(t)$, reflected wave stress $\sigma_R(t)$, and transmitted wave stress $\sigma_T(t)$ at time t. According to the one-dimensional wave transfer theory,[44] the dynamic stress $\sigma(t)$, axial strain $\varepsilon(t)$, and strain rate $\dot{\varepsilon}(t)$ can be expressed according to eqs 1−3.

$$\sigma(t) = \frac{A_e}{2A_s}[\sigma_I(t) - \sigma_R(t) + \sigma_T(t)] \quad (1)$$

$$\varepsilon(t) = \frac{1}{\rho_e C_e L_s}\int_0^t [\sigma_I(t) + \sigma_R(t) - \sigma_T(t)]dt \quad (2)$$

$$\dot{\varepsilon}(t) = \frac{1}{\rho_e C_e L_s}[\sigma_I(t) + \sigma_R(t) - \sigma_T(t)] \quad (3)$$

where A_e and ρe are the cross-sectional area and density of the Hopkinson pressure bar, respectively. A_s is the cross-sectional area of the specimen.

The objective is to pass a certain distance in the direction of the external force. During the impact load impact process, the sample also undergoes energy evolution under the action of an external load.[44] According to the integral rule, the work done by the incident wave stress $\sigma_I(t)$, reflected wave stress $\sigma_R(t)$, and transmitted wave stress $\sigma_T(t)$ at time t can be calculated, and the corresponding incident energy W_I, reflected energy W_R, and transmitted energy W_T can be expressed using eqs 4−6.

$$W_I = \frac{A_e}{\rho_e C_e}\int_0^\tau \sigma_I^2(t)dt \quad (4)$$

$$W_R = \frac{A_e}{\rho_e C_e}\int_0^\tau \sigma_R^2(t)dt \quad (5)$$

$$W_T = \frac{A_e}{\rho_e C_e}\int_0^\tau \sigma_T^2(t)dt \quad (6)$$

where τ is the stress wave duration. According to the law of conservation of energy,[45] the absorbed energy W_S can be calculated as eq 7, and the energy absorption rate T that characterizes the rupture of the sample can be expressed according to eq 8.

$$W_S = W_I - (W_R + W_T) \quad (7)$$

$$T = \frac{W_S}{W_I} \quad (8)$$

Table 5 summarizes the results of the energy characteristics of the UCCF and MCCF samples under impact loads. In a test

Table 5. Energy Characteristics of Cement Samples

sample	W_I (J)	W_R (J)	W_T (J)	W_S (J)	T (%)	strength (MPa)
control	60	29.88	26.98	3.14	5.23	12.16 ± 1.3
UCCF-0.2%	60	27.34	24.41	8.25	13.75	24.99 ± 1.5
UCCF-0.3%	60	24.75	19.66	15.59	25.98	37.01 ± 1.7
UCCF-0.4%	60	24.45	22.98	12.57	20.95	32.21 ± 1.8
UCCF-0.5%	60	27.19	23.46	9.35	15.58	26.19 ± 1.6
MCCF-0.2%	60	19.17	15.21	25.62	42.70	45.19 ± 1.5
MCCF-0.3%	60	9.64	6.05	44.31	73.85	62.27 ± 1.7
MCCF-0.4%	60	12.90	9.92	37.18	61.97	56.04 ± 1.6
MCCF-0.5%	60	16.55	12.71	30.74	51.23	49.57 ± 1.5

with a fixed air pressure of 0.5 MPa, an impact velocity of 10 m/s, and an incident energy of 60 J, the absorption energy W_S of the blank control was 3.14 J and the energy absorption rate T was 5.23%. In the UCCF group, with the increase in UCF loading from 0 to 0.5%, both W_S and T increased first and reached a maximum in UCCF-0.3%, where W_S = 15.59 J and T = 25.98%. In the MCCF group, the same trend was observed, but the maximum W_S and T were significantly higher than those in UCCF; i.e., W_s reached a peak in MCCF-0.3% at 44.31 J and T reached 73.85%. Considering that the duration of the impact test was very short, the number of internal defects directly affected the energy adsorption and release of the impact load,[46] which in turn affected the overall mechanical properties of the material. The bonding between UFC and the cement matrix was weak with the presence of some pores in between. As the loading of UCF increased, more pores could damage the integrity of the cement matrix and

https://doi.org/10.1021/acsomega.3c06486
ACS Omega 2024, 9, 7564−7574

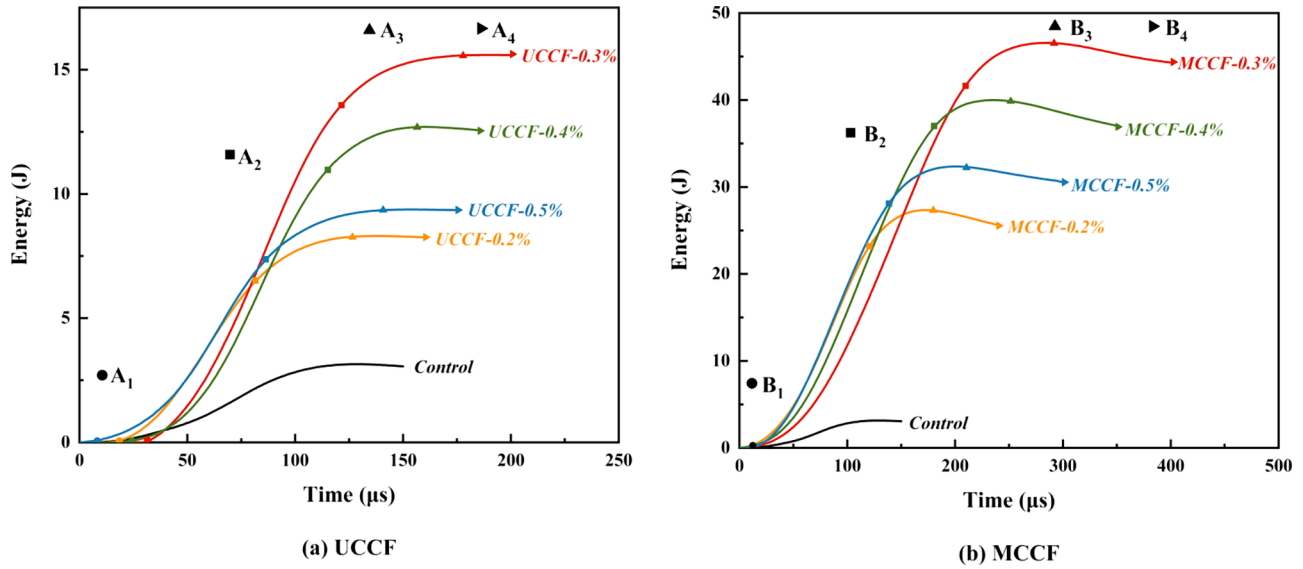

Figure 5. Time−energy diagrams of (a) UCCF and (b) MCCF under dynamic loading.

reduce the ability to absorb the impact load energy. However, in the case of MFC, with the number of hydrophilic groups increased, the binding capability of MCF to the cement matrix was significantly enhanced. As a result, both W_S and T increased. When the MCF loading was more than 0.3%, T and the peak strength of the MCCF decreased owing to the hardening of the matrix.

Figure 5 shows the time−energy diagrams of UCCF and MCCF samples with different CF loadings, wherein four stages can be identified for all nine samples during the impact process. The first stage is a compacting stage (0−A_1 and 0−B_1 sections). When the impact load was applied to the sample, the internal pores were compacted, leading to some minor energy fluctuation. In Figure 5a, with the increase in UCF loading, the pores between the cement matrix and UCF increased and the time of the compacting stage was prolonged. When the amount of UCF increased to 0.5%, the number of pores between UCF and the cement matrix increased rapidly, the transmission of impact load energy was more easily interrupted, and the time of the compacting stage was shortened. In Figure 5b, owing to the enhanced bonding ability between MCF and the cement matrix, the number of pores between MCF and the cement matrix was reduced and the transmission of the impact load energy was more coherent. The duration of the compacting stage remained almost unchanged when MCF loading was increased from 0 to 0.5%. The second stage is an energy accumulation stage (A_1−A_2 and B_1−B_2 sections). When the impact load was rapidly applied, the sample absorbed the energy of the impact load and the curve exhibited a linear upward trend. In Figure 5a, the UCCF-0.3% sample absorbed an energy of 15.59 J and bore the impact load for the longest time. Thus, it had the highest energy absorption rate and its peak strength was the highest. When the amount of UCF was too small or too large, the homogeneity of UCF in the cement matrix was reduced. The energy transfer of the impact load was easily interrupted, which was not favorable for energy accumulation. In Figure 5b, similarly, the sample with 0.3% MCF loading absorbed 44.31 J of impact energy with the longest impact load time. Thus, it had the highest energy absorption rate and the highest peak strength. The B_1−B_2 section was significantly longer than the A_1−A_2 section, indicating that the low-temperature plasma treatment was helpful in achieving coherent energy transfer during the impact process in terms of the accumulation of impact load energy. Moreover, the loading of 0.3% CFs could ensure a homogeneous distribution of CFs in the low-density cement system. The third stage is an instability stage, a convex-arc segment in the time−energy curve, i.e., A_2−A_3 and B_2−B_3 sections. In this stage, the energy accumulation approached the peak and the time rate of energy growth decreased slowly to 0. The cement stone samples were all in the critical state of transition from microcrack initiation to macrocrack propagation.[47] The last stage in the time−energy curve is an energy release stage (A_3−A_4 and B_3−B_4 sections). In this stage, microcracks were initiated with the impact load, adsorbed with the impact energy, and propagated inside the sample. When the cracks fully penetrated, the sample failed and the time−energy curve showed a descending segment. Comparing Figure 5a,b, the segment A_3−A_4 in the UCCF group was flat, while the segment B_3−B_4 in the MCCF group exhibited a downward trend. This showed that in the process of crack propagation, the resistance of the MCCF group to crack propagation was significantly higher than that of the UCCF group and the MCCF group provided more energy for crack propagation than the UCCF group specimens. When the loading of UCF was too small, it could not function as an effective skeleton for a low-density cement matrix, providing limited resistance to crack propagation.[48] When the loading of UCF was too large, the number of pores between UCF and the cement matrix increased because the bonding ability was insufficient.[49] In the case of MCF, when the amount of MCF is too small or too large, the homogeneity of MCF in the cement matrix was reduced, and the energy transfer of the impact load was easily interrupted, which was unfavorable for releasing the impact energy.

In summary, UCF had a smooth and hydrophobic surface with a weak bonding ability with the cement matrix. After low-temperature plasma treatment, the matrix bonding ability of MCF was significantly enhanced, which facilitated the coherent transfer of the impact load energy. Compared with the UCCF group, the MCCF group had fewer pores, a shorter compacting time, a longer duration of the energy accumulation process,

https://doi.org/10.1021/acsomega.3c06486
ACS Omega 2024, 9, 7564−7574

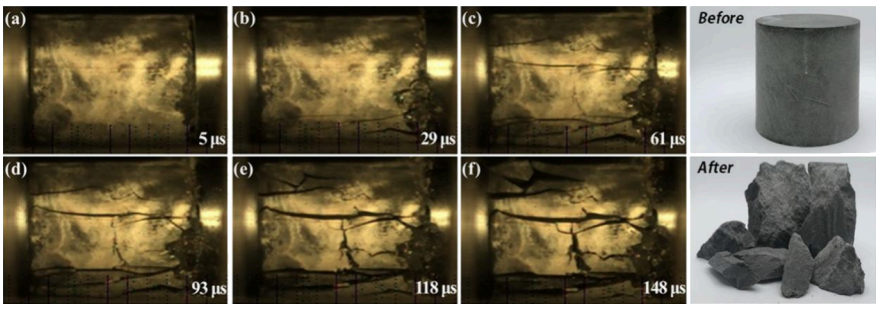

Figure 6. Crack propagation and image comparison of the blank control (a–c) before and (d–f) after the impact load.

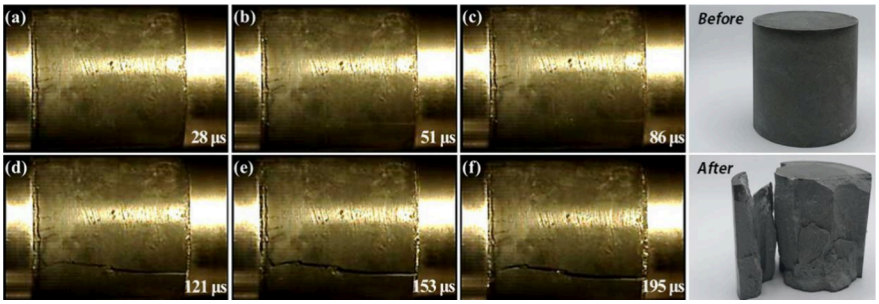

Figure 7. Crack propagation and image comparison of the UCCF sample (a–c) before and (d–f) after the impact load.

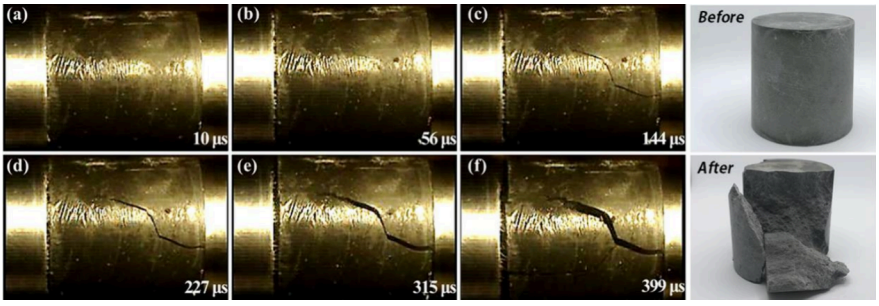

Figure 8. Crack propagation and image comparison of the MCCF sample (a–c) before and (d–f) after the impact load.

and a higher energy absorption rate, which provided energy for subsequent crack growth. In the CF low-density floating bead cement system, the optimal amounts of UCF and MCF were 0.3%. When the loading was insufficient or excessive, the energy utilization efficiency of the samples decreased under the impact load.

3.3.2. Dynamic Crack Derivation. Figure 6 shows the crack propagation process of the blank control and image comparison before and after the impact load. In Figure 6b–e, microcracks emerged at both ends and rapidly expanded to the middle of the sample rapidly. With the continuous loading of the impact, secondary cracks connected to the main crack and penetrated to form new cracks and localized damage. After the test, the cement matrix of the blank control was loose, and the floating beads fell off easily. It was difficult for the blank control to resist the huge energy of the impact load, and the peak strength and energy absorption efficiency were both low. Therefore, microcracks formed and expanded rapidly, eventually causing sample failure. The time for the blank control to bear the impact load is extremely short.

Figure 7 shows the crack propagation process of the UCCF sample and image comparison before and after the impact load. The main crack initiated at the interface between the sample and fixture and expanded along the axis of the sample, leading to an axial split eventually.[50] The specimen fragment size was large, and the number of fragments was small. As shown in Figure 7b–e, the main cracks emerged from one end and further expanded to the opposite end until penetration. No secondary cracks were observed. The sample was split under the action of an axial impact load, indicating that the resistance of UCF in the process of crack propagation was not sufficient. Compared to the blank control, UCCF played a supporting role as a skeleton in the cement matrix, which solved the pain point of the loose texture of the cement matrix to a certain extent. Because the surface of UCF was smooth and hydrophobic, the bonding ability with the cement matrix was weak. The gaps between UCF and the cement matrix resulted in poor energy absorption of the impact load; moreover, the resistance of the crack propagation was reduced, and the main crack split and penetrated along the axis. Thus, the UCCF sample bore the impact load for a short time.

Figure 8 shows the crack propagation process of the MCCF sample and the image comparison before and after impact load. The main crack was initiated at one end of the sample. The secondary cracks appeared during the axial expansion process, and shear cracks were also observed due to the direction shift.[51] The size of the specimen fragments was larger, and the fragments remained intact. In Figure 8b–e, the growth rate of

https://doi.org/10.1021/acsomega.3c06486
ACS Omega 2024, 9, 7564–7574

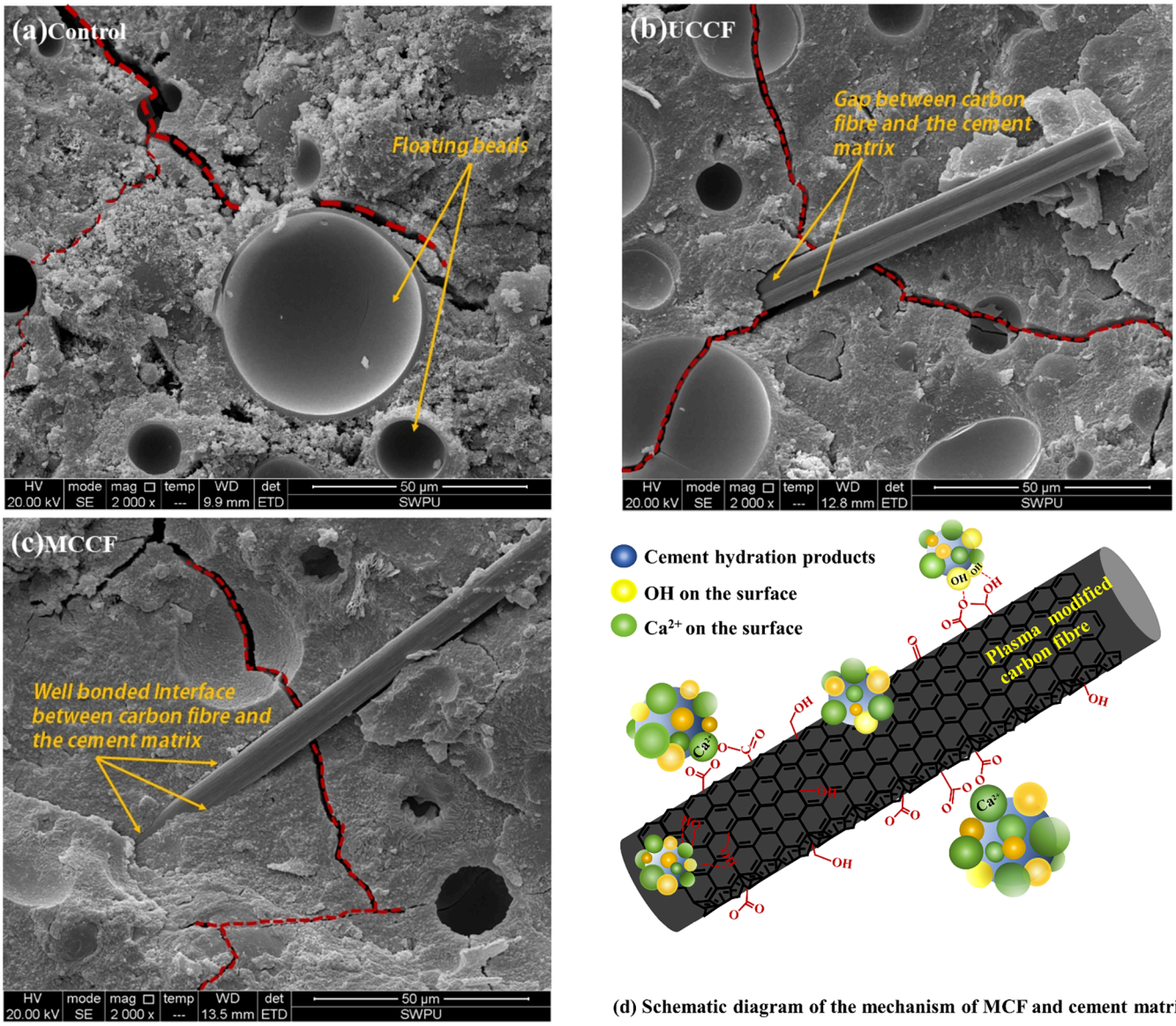

Figure 9. SEM images of the fracture surface of the (a) control sample, (b) UCCF sample, and (c) MCCF sample. (d) Schematic of the mechanism of the improved interaction between MCF and the cement matrix.

the main crack was relatively slow, indicating that the resistance of the crack in the axial expansion process was relatively large. The main crack was deflected in the shear direction in the middle of the sample,[52] implying that the damage was caused by a combined action of tensile and shear cracks. The above observation confirmed that the resistance of MCF is sufficient in the process of crack propagation. Compared to the blank control and the UCCF sample, the hydrophilic groups on the MFC surface enhanced the bonding strength with the cement matrix and were evenly distributed in the loose-textured cement matrix. In a low-density cement matrix, the MCF skeleton played the role of a stable support. Because the low-temperature plasma modification induced favorable chemical and physical properties on the MCF surface, the bonding ability with the low-density cement matrix was strong, and the energy efficiency for absorbing the impact load was improved. At the same time, MCF was closely combined with the low-density cement matrix, which increased the resistance of crack propagation. The main crack underwent noticeable crack deflection in the shear direction, and the damage to the sample was a common combination of tensile cracks and shear cracks. Therefore, the MCCF sample bore the impact load for a long time, and the peak strength under the impact load increased significantly.

In summary, as the hydrophilic groups on the surface of MCF increased due to low-temperature plasma treatment, the bonding force between the cement matrix and MCF was significantly enhanced, which was conducive to the coherent transfer of the impact load energy. In contrast to the blank control and the UCCF sample, MCF played a stable supporting role in the cement matrix and increased the crack propagation resistance and the energy consumption of the impact load through crack deflection. The higher efficiency of load energy utilization also extended the time that the sample could bear the impact load.

3.4. Fracture Micromorphology Analysis. Figure 9 shows SEM images of the fracture surfaces of the blank control, UCCF, and MCCF samples. In Figure 9a, the floating beads in the low-density cement stone fell off over a large area after the impact load. In addition, the cement matrix had a

https://doi.org/10.1021/acsomega.3c06486
ACS Omega 2024, 9, 7564−7574

loose texture, and the cracks between adjacent floating beads expanded easily. Figure 9b shows that the longitudinal surface of UCF was not tightly combined with the cement stone matrix with apparent voids in between, and the UCF in the cement matrix was in a pull-out state.[53] It was confirmed that UCF had weak bonding with the cement matrix and high mobility due to its smooth and hydrophobic surface. In this case, less impact load energy could be consumed during the crack propagation process. In Figure 9c, a small portion of the floating beads fell off, and MCF was embedded owing to a more substantial anchoring effect.[54] More cement hydration products were attached to the MCF surface, and there was no noticeable gap between them. As a result, the interface was strengthened, and the resistance to external dynamic loads and load energy consumption were significantly improved. It was confirmed that MCF acted as a skeleton in the low-density cement matrix and played a stable support role. The close bonding surface between MCF and the cement matrix improved the energy absorption efficiency of the cement. The resistance to crack propagation and the energy consumption of the crack deflection to generate shear cracks were higher, facilitating the consumption of the impact load energy and thereby improving the crack resistance, the peak strength, and the ability to resist external impact loads.

Figure 9d shows a schematic of the mechanism of the improved mechanical properties of MCCF. The purpose of plasma modification was to change the UCF surface from being hydrophobic to being hydrophilic. This could improve the bonding ability of UCF with the cement matrix and reduce the strength damage caused by ordinary modification treatment technology. The hydrophilic groups on the surface of the MCF closely combined with the Ca^{2+} of the cement matrix, and the MCF skeleton played a stable supporting role in the cement matrix. The stronger anchoring effect of MCF is conducive to coherent energy transfer during the impact process, which increases the crack propagation resistance and energy consumption of the impact load through crack deflection, thereby increasing the overall peak strength of the material under the impact load.

4. CONCLUSIONS

From the experimental results discussed above, we can draw the following conclusions:

1. The surface hydrophilicity of the CFs was significantly improved by low-temperature plasma treatment, and the content of hydrophilic groups (C−O, O−C═O) increased from 18.3 to 60.3%, which was beneficial for the anchoring effect of the CFs in the cement matrix.
2. Compared with the peak strength of the blank control (12.16 ± 1.3 MPa), UCCF and MCCF had relatively higher peak strengths. The maximum peak strengths were achieved as 37.01 ± 1.7 and 62.27 ± 1.7 MPa in the UCCF and MCCF groups, respectively, when 0.3% CFs were incorporated.
3. Compared to the blank control wherein the absorption energy was 3.14 J and the energy absorption rate was 5.23%, the absorbed energy and energy absorption rate were increased to 15.59 J and 25.98%, respectively, for the UCCF sample and further increased to 42.70 J and 73.85%, respectively, for the MCCF sample.
4. Better resistance to crack propagation was achieved when CFs were incorporated into the cement matrix. The UCCF sample split axially, and the crack resistance of the MCCF was significantly enhanced under the action of crack deflection.

AUTHOR INFORMATION

Corresponding Author

Xiaowei Cheng − *School of New Energy and Materials, Southwest Petroleum University, Chengdu 610500, China;* orcid.org/0000-0002-7975-7254; Phone: +86 028 83037437; Email: chengxw@swpu.edu.cn; Fax: +86 028 83037406

Authors

Yong Ma − *Petro China Southwest Oil and Gas Field Company, Chengdu 610051, China*

Jianhua Guo − *Petro China Southwest Oil and Gas Field Company, Chengdu 610051, China*

Sen Liu − *Petro China Southwest Oil and Gas Field Company, Chengdu 610051, China*

Yangsong Wang − *Petro China Southwest Oil and Gas Field Company, Chengdu 610051, China*

Jingxuan Cai − *School of New Energy and Materials, Southwest Petroleum University, Chengdu 610500, China*

Complete contact information is available at: https://pubs.acs.org/10.1021/acsomega.3c06486

Notes

The authors declare no competing financial interest.

ACKNOWLEDGMENTS

This research was supported by the Scientific Research and Technology Development Project of Petro China Southwest Oil and Gas Field Company: Research on Anti-pollution Technology of Ultra-deep Liner Cementing Slurry (Project No.: 20230302-19). We would like to thank the Advanced Cementing Materials Research Centre of Southwest Petroleum University.

REFERENCES

(1) Deng, K.; Liu, W.; Xia, T.; et al. Experimental study the collapse failure mechanism of cemented casing under non-uniform load. *Eng. Failure Anal.* **2017**, *73*, 1.

(2) Wang, W.; Taleghani, A. D. Three-dimensional analysis of cement sheath integrity around Wellbores. *J. Pet. Sci. Eng.* **2014**, *121*, 38.

(3) Xi, Y.; Li, J.; Liu, G.; et al. A new numerical investigation of cement sheath integrity during multistage hydraulic fracturing shale gas wells. *J. Nat. Gas Sci. Eng.* **2018**, *49*, 331.

(4) Sarmah, P.; N., Al Tawat, Yadav, P.; Agrawal, G. High Compressive Strength, Ultra-Lightweight and Lightweight Cement − Formulated with Raw Material Locally Available in Saudi Arabia; *SPE Kingdom of Saudi Arabia Annual Technical Symposium and Exhibition* Society of Petroleum Engineers, Dammam, Saudi Arabia, 2016 DOI: 10.2118/182736-MS.

(5) Zeng, J.; You, F. A new type of low density cement slurry suitable for sandstone formation. *IOP Conf. Ser.: Mater. Sci. Eng.* **2021**, *1133* (1), No. 012005.

(6) Sarmah, P.; Yadav, P.; Agrawal, G. High-Strength Lightweight Cement Optimized for Weak Formations - Use of Local Raw Material Improves Performance and Operational Latitude; *SPE Oil & Gas India Conference and Exhibition* Society of Petroleum Engineers, Mumbai, India, 2015 DOI: 10.2118/178038-MS.

(7) Sauki, A.; Juanda, M. I.; Azizi, A.; et al. Performance Evaluation of Lightweight Oilwell Cements. *Adv. Mater. Res.* **2015**, *1119*, 657.

(8) Anya, A. Lightweight and Ultra-Lightweight Cements for Well Cementing − A Review; *SPE Western Regional Meeting* Society of Petroleum Engineers, Garden Grove, California, USA, 2018 DOI: 10.2118/190079-MS.
(9) Cheng, X. W.; Khorami, M.; Shi, Y.; Liu, K. Q.; Guo, X. Y.; Austin, S.; Saidani, M. A new approach to improve mechanical properties and durability of low-density oil well cement composite reinforced by cellulose fibres in microstructural scale. *Constr. Build. Mater.* **2018**, *177*, 499−510.
(10) Nelson, E. B.; Guillot, D. *Well Cementing*, Schlumberger, Sugar Land, Tex, 2006.
(11) Sugumaran, M. Study on Effect of Low Calcium Fly Ash on Geopolymer Cement for Oil Well Cementing; *SPE/IATMI Asia Pacific Oil & Gas Conference and Exhibition* Society of Petroleum Engineers, Nusa Dua, Bali, Indonesia, 2015 DOI: 10.2118/176454-MS.
(12) Wang, C.; Chen, X.; Wang, L.; Ma, H.; Wang, R. A novel self-generating nitrogen foamed cement: the preparation, evaluation and field application[J]. *Nat. Gas Sci. Eng.* **2017**, *44*, 131−139.
(13) Mata, C.; Calubayan, A. Use of Hollow Glass Spheres in Lightweight Cements-Selection Criteria; *SPE Asia Pacific Oil & Gas Conference and Exhibition* Society of Petroleum Engineers, Perth, Australia, 2016 DOI: 10.2118/182399-MS.
(14) Liu, K. Q.; Cheng, X. W.; Zhang, X. G.; et al. Design of low-density cement optimized by cellulose-based fibre for oil and natural gas wells. *Powder Technol.* **2018**, *338*, 506.
(15) Cheng, X. W.; Khorami, M.; Shi, Y.; et al. A new approach to improve mechanical properties and durability of low-density oil well cement composite reinforced by cellulose fibres in microstructural scale. *Constr. Build. Mater.* **2018**, *177*, 499.
(16) Li, M.; Liu, M.; Yang, Y.; et al. Mechanical properties of oil well cement stone reinforced with hybridfiber of calcium carbonate whisker and carbonfiber[J]. *Pet. Explor. Dev.* **2015**, *42*, 104−111.
(17) Zhang, W.; Zhang, Y.; Liu, B. Hybrid effect of basalt fiber and carbon fiber on the mechanical properties and microstructure of oil well cement. *Constr. Build. Mater.* **2021**, *286*, No. 122696.
(18) Cheng, X.; Huang, S.; Guo, X.; et al. Crumb waste tire rubber surface modification by plasma polymerization of ethanol and its application on oil-well cement. *Appl. Surf. Sci.* **2017**, *409*, 325.
(19) Gao, J.; Wang, Z.; Zhang, T.; et al. Dispersion of carbon fibers in cement-based composites with different mixing methods. *Constr. Build. Mater.* **2017**, *134*, 220−227.
(20) Lee, H.; Ohsawa, I.; Takahashi, J. Effect of plasma surface treatment of recycled carbonfiber on carbonfiber-reinforced plastics (CFRP) interfacial properties[J]. *Appl. Surf. Sci.* **2015**, *328*, 241−246.
(21) Yu, Y.; Fu, J.; Zhang, C.; et al. Mechanical Properties and Enhancement Mechanism of Oil-Well Cement Stone Reinforced with Carbon Fiber Surfaces Treated by Concentrated Nitric Acid and Sodium Hypochlorite. *Int. J. Polym. Sci.* **2020**, *2020*, 1.
(22) Xiong, S.; Zhao, Y.; Wang, Y.; et al. Enhanced interfacial properties of carbon fiber/epoxy composites by coating carbon nanotubes onto carbon fiber surface by one-step dipping method. *Appl. Surf. Sci.* **2021**, *546*, No. 149135.
(23) Chen, H.; Cai, Q.; Wu, J.; et al. Interfacial enhancement of carbon fiber/nylon 12 composites by grafting nylon 6 to the surface of carbon fiber. *Appl. Surf. Sci.* **2018**, *441*, 538.
(24) Huang, S.; Cheng, X.; Guo, X.; et al. Ethanol plasma-induced polymerization of carbon fiber surface for improving mechanical properties of carbon fiber-reinforced lightweight oil well cement. *Appl. Surf. Sci.* **2019**, *497*, No. 143765.
(25) Gilman, A. B.; Piskarev, M. S.; Kuznetsov, A. A.; et al. Modification of ultrahigh-molecular-weight polyethylene by low-temperature plasma (review). *High Energy Chem.* **2017**, *51* (2), 136.
(26) Zhang, C.; Li, Y.; Cheng, X.; et al. Effects of plasma-treated rock asphalt on the mechanical properties and microstructure of oil-well cement. *Constr. Build. Mater.* **2018**, *186*, 163.
(27) Cheng, X.; Liu, K.; Zhang, X.; et al. Integrity changes of cement sheath due to contamination by drilling fluid. *Adv. Cement Res.* **2018**, *30* (2), 47.
(28) Shiyan, S. I.; Shutov, D. V.; Fesenko, M. Y.; et al. Application of Drilling Oscillator During Drilling Directional Wells in the Field Conditions of Gubkinskoye Oil and Gas Field While Drilling No. 2156. *IOP Conf. Ser.: Earth Environ. Sci.* **2021**, *720* (1), No. 012071, DOI: 10.1088/1755-1315/720/1/012071.
(29) Feng, S.; Zhou, Y.; Wang, Y.; et al. Experimental research on the dynamic mechanical properties and damage characteristics of lightweight foamed concrete under impact loading. *Int. J. Impact Eng.* **2020**, *140*, No. 103558.
(30) Deng, Q.; Zhang, H.; Chen, A.; et al. Effects of perforation fluid movement on downhole packer with shock loads. *J. Pet. Sci. Eng.* **2020**, *195*, No. 107566.
(31) American Petroleum Institute (API), *API 10B-2: Recommended prectice for testing well cements*, Second Edition, 2013.
(32) Liu, P.; Hu, D.; Wu, Q.; et al. Sensitivity and uncertainty analysis of interfacial effect in SHPB tests for concrete-like materials. *Constr. Build. Mater.* **2018**, *163*, 414.
(33) Li, J.; Zhao, J.; Gong, S. Y.; et al. Mechanical anisotropy of coal under coupled biaxial static and dynamic loads. *Int. J. Rock Mech. Min. Sci.* **2021**, *143*, No. 104807.
(34) Ulus, H.; Üstün, T.; Sahin, Ö. S.; et al. Low-velocity impact behavior of carbon fiber/epoxy multiscale hybrid nanocomposites reinforced with multiwalled carbon nanotubes and boron nitride nanoplates. *J. Compos. Mater.* **2016**, *50* (6), 761.
(35) Huang, Y. Effect of surface treatment on surface characteristics of carbon fibers and interfacial bonding of PMMA resin composites. *Compos. Interfaces* **2019**, *26* (8), 679 DOI: 10.1080/09276440.2018.1526593.
(36) Johansson, L. S.; Campbell, J. M.; Koljonen, K.; et al. Evaluation of surface lignin on cellulose fibers with XPS. *Appl. Surf. Sci.* **1999**, *144-145*, 92.
(37) Cheng, X.; Qin, D.; Chen, Z.; et al. Mechanical response and crack propagation of oil well cement under dynamic and static loads. *J. Adhes. Sci. Technol.* **2019**, *33* (15), 1658.
(38) Khan, M. Z. N.; Hao, Y. F.; Hao, H.; et al. Experimental evaluation of quasi-static and dynamic compressive properties of ambient-cured high-strength plain and fiber reinforced geopolymer composites. *Constr. Build. Mater.* **2018**, *166*, 482.
(39) Li, X.; Lok, T.; Zhao, J. Dynamic Characteristics of Granite Subjected to Intermediate Loading Rate. *Rock Mech. Rock Eng.* **2005**, *38* (1), 21.
(40) Yu, H.; Lei, Y.; Pei, C.; Wei, L.; Zhu, J. H.; Xing, F. Enhancing the mechanical and functional performance of carbon fiber reinforced cement mortar by the inclusion of a cost-effective graphene nanofluid additive. *Cem. Concr. Compos.* **2022**, *134*, No. 104777.
(41) Luo, L.; Li, X.; Tao, M.; et al. Mechanical behavior of rock-shotcrete interface under static and dynamic tensile loads. *Tunnelling Underground Space Technol.* **2017**, *65*, 215.
(42) Han, Z.; Li, D.; Zhou, T.; et al. Experimental study of stress wave propagation and energy characteristics across rock specimens containing cemented mortar joint with various thicknesses. *Int. J. Rock Mech. Min. Sci.* **2020**, *131*, No. 104352.
(43) Zhu, J.; Wei, J.; Yu, Q.; et al. Hybrid Effect of Wollastonite Fiber and Carbon Fiber on the Mechanical Properties of Oil Well Cement Pastes. *Adv. Mater. Sci. Eng.* **2020**, *2020*, 1.
(44) Li, D.; Han, Z.; Sun, X.; et al. Dynamic Mechanical Properties and Fracturing Behavior of Marble Specimens Containing Single and Double Flaws in SHPB Tests. *Rock Mech. Rock Eng.* **2019**, *52* (6), 1623.
(45) Han, Z.; Li, D.; Zhu, Q.; et al. Dynamic Fracture Evolution and Mechanical Behavior of Sandstone Containing Noncoplanar Elliptical Flaws under Impact Loading. *Adv. Civil Eng.* **2018**, *2018*, 1.
(46) Guo, Y. B.; Gao, G. F.; Jing, L.; et al. Response of high-strength concrete to dynamic compressive loading. *Int. J. Impact Eng.* **2017**, *108*, 114.
(47) Zhang, C.; Cai, J.; Cheng, X.; et al. Interface and crack propagation of cement-based composites with sulfonated asphalt and plasma-treated rock asphalt. *Constr. Build. Mater.* **2020**, *242*, No. 118161.

https://doi.org/10.1021/acsomega.3c06486
ACS Omega 2024, 9, 7564−7574

(48) Kim, J. H.; Han, J. H.; Hong, S. K.; et al. Effect of plasma surface modification on pullout characteristics of carbon fiber-reinforced cement composites. *Carbon Trends* **2021**, *3*, No. 100030, DOI: 10.1016/j.cartre.2021.100030.
(49) Liu, K.; Cheng, X.; Ma, Y.; et al. Analysis of interfacial nanostructure and interaction mechanisms between cellulose fibres and calcium silicate hydrates using experimental and molecular dynamics simulation data. *Appl. Surf. Sci.* **2020**, *506*, No. 144914.
(50) Wang, Q.; Li, W.; Xie, H. Dynamic split tensile test of Flattened Brazilian Disc of rock with SHPB setup. *Mech. Mater.* **2009**, *41* (3), 252.
(51) Xie, Y. J.; Fu, Q.; Zheng, K. R.; et al. Dynamic mechanical properties of cement and asphalt mortar based on SHPB test. *Constr. Build. Mater.* **2014**, *70*, 217.
(52) Wang, S.; Le, H. T. N.; Poh, L. H.; et al. Effect of high strain rate on compressive behavior of strain-hardening cement composite in comparison to that of ordinary fiber-reinforced concrete. *Constr. Build. Mater.* **2016**, *136*, 31.
(53) Zhang, C.; Cai, J.; Xu, H.; et al. Mechanical properties and mechanism of wollastonite fibers reinforced oil well cement. *Constr. Build. Mater.* **2020**, *260*, No. 120461.
(54) Wang, R.; Li, J.; Zhang, T.; et al. Chemical interaction between polymer and cement in polymer-cement concrete. *Bull. Pol. Acad. Sci. Tech. Sci.* **2016**, *64* (4), 785.

https://doi.org/10.1021/acsomega.3c06486
ACS Omega 2024, 9, 7564−7574